Cryogenic Process to Elaborate Poly(ethylene glycol) Scaffolds. Experimental and Simulation Studies

8 AUTHORS, INCLUDING:

Irais Quintero
Universidad de Guanajuato

11 PUBLICATIONS   **101** CITATIONS

SEE PROFILE

Josué D. Mota-Morales
Consejo Nacional de Ciencia y Tecnología

19 PUBLICATIONS   **78** CITATIONS

SEE PROFILE

Eduardo Elizalde
Autonomous University of Queretaro

12 PUBLICATIONS   **83** CITATIONS

SEE PROFILE

Diana G. Zarate
Center for Research and Advanced Studies of t…

4 PUBLICATIONS   **8** CITATIONS

SEE PROFILE

Cryogenic Process to Elaborate Poly(ethylene glycol) Scaffolds. Experimental and Simulation Studies

Iraís A. Quintero Ortega,[†] Josué D. Mota-Morales,[‡] Eduardo A. Elizalde Peña,[‡] Diana G. Zárate-Triviño,[‡] Yair A. De Santiago,[‡] Arturo Ortiz,[§] Beatriz García Gaitan,[‖] Isaac C. Sanchez,[⊥] and Gabriel Luna-Bárcenas[‡,*]

[†]Sciences and Engineering Division, Universidad de Guanajuato, Campus León, Loma del Bosque #103, Col. Lomas del Campestre, 37150 León, México

[‡]Cinvestav Querétaro, Libramiento Norponiente #2000, Frac. Real de Juriquilla, 76230 Querétaro, México

[§]Department of Sciences and Engineering, Universidad Autónoma de Tlaxcala, Tlaxcala, Tlax., México

[‖]Postgraduate Studies and Research Division, Instituto Tecnológico de Toluca, Metepec, Edo. Méx., México

[⊥]Department of Chemical Engineering, The University of Texas at Austin, Austin, Texas 78712, United States

ABSTRACT: Porous materials are of great importance because of their multiple applications in pharmacy, catalysis, and biomedicine among others. Ice segregation induced self-assembly (ISISA) is a cryogenic technique that uses the ice as a template that forms upon immersion of a polymer solution into liquid nitrogen to obtain highly porous materials. Some highlights of this technique are its versatility, simplicity, and control over the final structure of the produced material; besides, no organic solvents are used during the process, and the material can be used without the need of further cleaning. In this contribution, the elaboration of scaffolds using a poly(ethylene glycol) aqueous solutions by an ice-template process has been studied from experimental and theoretical viewpoints. The experimental study of the process parameters, such as immersion velocity and a prescribed freezing front on the morphology, was carried out. Simulations were performed to understand the ISISA process by calculating temperature profiles and pore size as a function of time. The most important result of this study was the effect of freezing rate on pore size. The technique was optimized such that a recipe is proposed to form materials with 1−100 μm pore sizes.

1. INTRODUCTION

Porous materials are important because of their diverse technological applications, which include organic electronics, microfluidics, molecular filtration, nanowires, and tissue engineering.[1,2] They are also used in biomedical applications, for example, artificial skin, drug delivery systems, bone reconstruction, and tissue engineering; for each application, the material must satisfy certain requirements (i.e. pore sizes from 50 to 250 μm are needed in bone reconstruction) compressibility and pore interconnection.[3]

A scaffold is a porous material normally used as support; techniques for its production include three-dimensional (3D) impression and stereolithography, which are used to produce controlled structures. However, such structures are not viable at a micrometer scale. Other techniques include the use of phase separation, gas foaming, supercritical fluids, and fiber cross-linking when it is not necessary to strictly control the material's geometry. The use of solvents or the generation of side products during scaffold formation generates the need of material's cleaning before it can be used as cellular support.[4]

Unidirectional freezing had been used to produce different materials such as silica fibers, honeycomb structures, micrometric porous materials, cryogels, etc. Some highlights of this technique are its versatility, simplicity, and control over the final structure of the produced material. Additionally, no organic solvents are used during the process, and the material can be used without the need of further cleaning. The main drawback

of unidirectional freezing is the heterogeneity of the formed material. Materials produced with this technique are named cryogels and can be used as scaffolds in many of the above technological applications.

One of the first systems studied was the production of 3D alginate scaffolds using three different freezing techniques.[5] Another 3D structure obtained with a cryogenic process includes polymers and nanoparticles.[1] Deville et al. demonstrated that the ice-template process can be used to develop sophisticated porous materials.[6]

The ice segregation induced self assembly (ISISA) process consists of the unidirectional freezing of an aqueous solution by immersing into a liquid nitrogen (LN) bath. The ice structure acts as the pattern for the solute, and the crystal structure of ice does not allow the inclusion of impurities.[31] The material obtained after freeze-drying show macroporosity that corresponds to the empty areas where ice crystals resided.

Scaffolds with a wide variety of compositions and good structural control can be prepared with the ice-template process. However, materials do not present a homogeneous pore distribution. Three different zones can be observed in the freezing direction depending upon the pore and shape sizes;

these zones are known as dense, cellular, and lamellar zones.[32] The main drawback of the technique is the heterogeneity in the material that leads to large quantities of waste material; that is, it does not allow the use of the entire material due to the heterogeneity of the pore size and interconnectivity; these two properties are of great importance in biomedical applications.

Recent materials produced with this cryogenic technique include silica gel microhoneycombs,[7] porous hydroxyapatite scaffolds,[8] silica nanoparticles with liposomes,[9] gold nanoparticles in chitosan scaffold,[10] silver nanowires/poly(vinyl alcohol) (PVA) scaffold,[11] starch monoliths,[12] biporous chitosan,[13] inverse opal scaffolds of chitosan,[14] encapsulated bacteria in silica gel,[15] PVA with pig liver esterase incorporated to silica gel,[16] PVA scaffold with *E. coli* bacteria,[17] multiwall carbon nanotubes (MWCNT) scaffold with *E. coli* bacteria,[18] MMWCNT scaffold mineralized with calcium phosphate,[19] MMWCNT scaffold for tissue engineering,[20] graphene oxide for fuel cell,[21] graphene oxide aerogels,[22] biodegradable graphene oxide monoliths,[23] carbon nanofibers by carbonization of lignine scaffolds,[24] nanocomposites,[25,26] porous alumina,[27] and PVA scaffolds for drug delivery.[28−30]

Despite all the advantages offered by this technique, the interplay of thermodynamics, kinetics, and crystallization are not well understood. It only had been studied from the experimental viewpoint. The first attempt to model this process came from Nakagawa et al., who simulated the temperature profile for the freezing process of pharmaceuticals in a glass vial;[33] the same model was used to simulate two different freezing processes (contact and immersion) to produce solid foams from a carbon nanotube suspension.[34] The temperature was measured through three thermocouples placed in different zones of the sample (surroundings, center, and wall), and the results were compared with the temperature obtained from the model showing good agreement. However, modeling of the mean ice crystal size and morphology was simulated with an empirical correlation. It would be desirable to model crystallization using population balances, for instance.

In this contribution, the elaboration of poly(ethylene glycol) (PEG) scaffolds using a poly(ethylene glycol) aqueous solutions by an ice-template process has been studied from experimental and theoretical viewpoints. One of the key factors to optimize a cryogenic technique is the freezing front rate, because this parameter controls pore size and interconnectivity. For simulation purposes, a model is proposed to simulate temperature profile and ice crystal size distributions along the sample as a function of time.

The main objective of this study is to give a deeper understanding of the phenomena occurring during the ISISA process and to optimize the technique by minimizing the heterogeneity of the material.

2. EXPERIMENTAL SECTION

2.1. Scaffold Elaboration. Poly(ethylene glycol) from Sigma-Aldrich (M_w = 35 kDa, melting point 331 K) was used as received. Dissolution of PEG was prepared adding 12.5 g PEG to 87.5 g of distilled water (12.5% w/w). The PEG solution was placed in a 1 mL insulin syringe (with marks from 0 to 100, see Figure 1b), and then it was immersed into LN (contained in a Dewar flask) until the freezing front reach the end of the syringe. Subsequent lyophilization of the frozen PEG solution was performed (Labconco model FreeZone4.5).

Four freezing techniques were designed and studied:
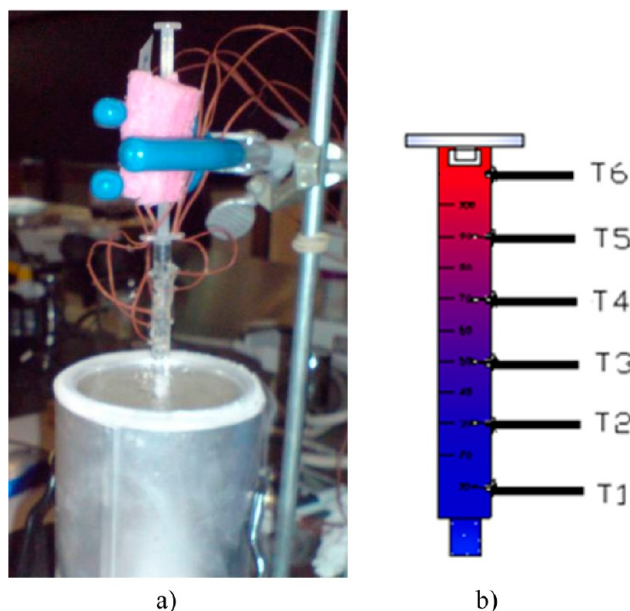
Figure 1. ISISA process and schematic representation of the thermocouples placed on the sample.

1. LCI 10−30 (linear-controlled-immersion 10−30): in this case, the LN liquid level was kept constant during the entire process. This was achieved by slowly pouring LN into the Dewar flask to compensate for the evaporated LN, thus allowing a constant LN liquid level. The process starts by quickly immersing the tip of the syringe until mark 10 is leveled off with the LN meniscus. This will trigger the freezing front upward. This is visually observed by the "whitening" of the solution. Once the freezing front develops and reaches the mark 30 (see Figure 1b), the syringe is quickly immersed into LN until the mark 20 levels off with the LN meniscus and the freezing front keeps moving upward. This procedure was repeated once the freezing front moved two 10 marks. Once the syringe position reaches the mark 60 that levels off with the LN meniscus, the syringe position is locked and the freezing front freely moves upward until the whole polymer solution is frozen.

2. LCI: this technique is similar to LCI 10−30. However, there is an exception: once the syringe reaches the mark 60 and the freezing front reaches the mark 80, the syringe was again immersed into the LN until reaching the mark 70. This procedure was repeated until the final position of the syringe is mark 80.

3. CI-vapors (controlled immersion with vapors): in this case, the process starts by keeping the level of LN constant and immersing the sample to the 10 mark on the syringe. This triggers the freezing front until the mark 50 is reached. From this moment, the level of LN was not kept constant and the immersion of the sample was initiated parallel to the descending of the LN level (due to LN evaporation). This procedure continues until the freezing front reaches the end of the sample. It is noteworthy that the tip of the syringe (mark 10) is immersed in LN at all times.

4. CI (constant immersion): in this technique, the LN level was kept constant and the sample was immersed into the

LN at a constant rate (0.015−0.24 mm/s) until the freezing front reaches the end of the sample.

2.2. Morphology and Temperature Profiles. Morphology characterization was studied with the semistatic techniques. The frozen solution inside the syringe was sectioned always keeping it frosted. All the sections obtained were freeze-dried. Morphology was studied with scanning electron microscopy (SEM Philips XL30 ESEM).

Temperature profiles were measured for all samples processed with LCI 10−30, LCI, CI-vapors, and CI. Figure 1 shows a picture of the experimental setup.

To obtain the experimental temperature profile, six thermocouples K-type were placed at the center of the sample holder at different heights from bottom to top (T1 = 5.7 mm, T2 = 17.1 mm, T3 = 28.5 mm, T4 = 39.9 mm, T5 = 51.3 mm, and T6 = 62.7 mm). In Figure 1b, it can observe a schematic representation of the thermocouples position along the sample. The temperature was measured every second through an acquisition data card (National Instruments, module USB 9213, 16-ch TC, 24-bit C) on which 16 thermocouples can be connected. The acquisition card was interfaced to a computer for the storage and data analysis.

3. MODELING

Although the modeling of ice crystal formation has been studied in different areas, Nakawaga et al.[33] were the first in model a cryogenic process similar to the studied in this work. They divided the system into the freezing and cooling steps to simulate a temperature profile. The same model was used to simulate the immersion of carbon nanotube aqueous solution into a cryogenic bath to form solid foams[34] and most recently in the freeze-dried of poly(epsilon-caprolactone) nanocapsules.[35]

In this work, a mixed methodology is proposed to obtain a mathematical representation of the ISISA process.

3.1. Model Description. The Stefan problem was used to model the formation of ice; nucleation and crystal growth are calculated with a population balance method and with an Eulerian two-phase model that considers heat and mass transfer between the water-PEG solution to the liquid water or ice.

3.1.1. Stefan Approach. A simplified Stefan approach with a moving boundary in which solid and liquid are considered two distinct phases and no mushy zone is tracked help us to solve the problem of ice formation. The principal equations are presented as follows.

For the liquid phase,

$$\rho_L \frac{\partial}{\partial t} Cp_L T_L = k'_{el} \nabla^2 T - a_{wall} h_{wall} (T_L - T_{wall}) \tag{1}$$

For the solid phase,

$$\rho_S \frac{\partial}{\partial t} Cp_S T_S = k'_{es} \nabla^2 T - a_{wall} h_{wall} (T_S - T_{wall}) \tag{2}$$

In the front tracking equation, $\xi(x)$ is the location of the liquid−solid boundary h_M is the latent heat of freezing, $\partial \xi / \partial t$ is the velocity of advancement of the interface, and T_m is the melting temperature.

Stefan condition for front tracking:

$$k'_{es} \frac{\partial T_S}{\partial x} + k'_{el} \frac{\partial T_L}{\partial x} + \rho_M \Delta h_M \frac{\partial \xi}{\partial t} = 0 \tag{3}$$

3.1.2. Eulerian-Population Balance Model. The population balance (PB) equation used is the standard method as described in Ramkrishna.[36] Only nucleation (birth) and growth terms are included in the PB equation.

3.1.2.1. Nucleation. The number and size of the nucleated crystals were obtained by a gamma function with λ and κ parameters fitted from experimental data;

$$f_X(x; \kappa, \lambda) = \frac{e^{-x/\lambda} x^{\kappa-1}}{\Gamma(\kappa) \lambda^\kappa}; \quad x > 0, \ \kappa > 0, \ \lambda > 0 \tag{4}$$

As a first approximation, the nucleation is considered homogeneous. The nucleation rate reached its stationary value at the temperature T_c, and it is denoted by $J_0(T_c)$. The following definitions are used: $x(t)$ is the fraction of crystallized water at time t, $m(t)$ is the mass of crystallized water at time t, M is the total amount of water dispersed, ρ is the density, and δN_v and $\delta \acute{N}_v$ are the number of uncrystallized droplets at $t = 0$ and $t = t$, respectively; those volumes are included between V and $V + \delta V$. $\delta \acute{N}_v$ is related to δN_v as follows:

$$\delta \acute{N}_v = \delta N_v \exp(J_0 V t) \tag{5}$$

It is considered that melting temperature T_m is constant such that the thickness is also constant.

3.1.2.2. Growth. A model based in an extended Flory−Huggins (FH) theory applied to the PEG-water system was used to account for the phase change in the system:

$$\frac{\Delta G_{mix}}{kT} = N_{PEG} \ln \varphi_{PEG} + N_W \ln(1 - \varphi_{PEG})$$
$$+ \chi \varphi_{PEG}(1 - \varphi_{PEG})(N_{PEG} r_{PEG} + N_W r_W) \tag{6}$$

In this equation, ϕ_{PEG} and $1 - \phi_{PEG}$ are the volume fraction of PEG and water in the solid mixture, respectively.

Thermodynamic instability that leads to phase separation occurs at

$$\left(\frac{\partial^2 \Delta G_{mix}}{\partial \varphi_1^2} \right)_{T,P} < 0$$

When the FH equation is applied to the stability criterion,

$$\frac{1}{r_{PEG} \varphi_{PEG}} + \frac{1}{r_W \varphi_W} - 2\chi = 0 \tag{7}$$

A common extension of the FH equation is obtained when the interaction parameter χ is expressed as a temperature dependent polynomial with constants α, β, and γ, all fitted from experimental data:

$$\chi = \frac{\alpha}{T} + \beta + \gamma T \tag{8}$$

This formulation allows the calculation of the volume fraction of liquid water ϕ_W in the concentrated polymer solution with the FH equation when temperature changes.

While the method is simple and predicts the PEG−water system separation, the size of the pores is not realistic; therefore, a mass transfer term is included in the model.

3.1.3. Mass and Heat Transfer for the Eulerian Model. In the Eulerian model, the concentrated PEG solution and the water are treated as separate phases. As the freezing front advances ice structure will be formed, after the freeze-drying process the space filled by ice will be empty, given as result a porous material. The model has two ways to obtain the porous

fraction; the second moment of the population balance and mass transfer by the Eulerian model. The reason for using both the Eulerian and population balance is that it is expected that each model will provide important information on the phenomena: ice formation with the population balance equation and mass transfer with the Eulerian part.

For a two-dimensional, nonflow, time dependent system, the equations derived for each component, PEG solution and water phases, can be written as follows:

Concentration of water in the PEG−water solution phase,

$$\frac{\partial}{\partial t}\varepsilon_{Sol}C_{Sol} + D_{WP}\nabla^2 \cdot \varepsilon_{Sol}C_{Sol} - k_m\rho_{Sol}(\varphi_{Sol} - \varphi_W) = 0 \tag{9}$$

Concentration of water (ice),

$$\frac{\partial}{\partial t}\varepsilon_W C_W + D_{WP}\nabla^2 \cdot \varepsilon_W C_W + k_m\rho_W(\varphi_{Sol} - \varphi_W) = 0 \tag{10}$$

In these equations, ε_W and ε_{Sol} are the volume fraction of the water and concentrated solution phases; ϕ_W and ϕ_{Sol} are the volume fraction of water and PEG−water solution in each phase calculated with the FH model.

$$\varepsilon_W + \varepsilon_{Sol} = 1 \tag{11}$$

Before freezing, the heat transfer in the mixture is

$$\rho_M \frac{\partial}{\partial t}Cp_M T_M = k'_{ea}\nabla^2 T - a_{wall}h_{wall}(T_M - T_{wall}) \tag{12}$$

where T_{wall} is the temperature at the wall, which is constant and set to an experimentally measured value, a_{wall} and h_{wall} are the heat transfer area and coefficient, both obtained from measured data.

3.2. Model Implementation. Mixture separation, nucleation, and crystal growth are modeled with a population balance method imbedded in an Eulerian two phase model that allows heat and mass transfer between concentrated water−PEG solutions to the decreasingly diluted solution. Each solution is treated as a separate phase. Solidification with freezing front tracking problem is solved using a simplified Stefan approach with a moving boundary model in which solid and liquid are also considered two distinct phases. The set of equations were solved using the commercial software (FLUENT) with finite volume method in an axis-symmetrical domain. Cylindrical geometry was used.

The two phase Eulerian−Population balance model is solved in a first time step, and then, the solution of the two phases Stefan problem procedure is attempted in the next time step using the temperature and phase values from the previous step. After solving the two problems, the sequence is repeated for the n time steps required.

3.3. Parameter Estimation. Pure PEG and PEG−water thermal properties are difficult to find as PEG is manufactured in a wide variety of molecular weights ranging from 1 to over 100 KDa. For this reason, thermodynamic data on PEG-35 KDa are scarce and difficult to estimate.

In this work, the Flory−Huggins theory and UNIQAC method were applied to estimate the properties of the mixture.

Experimental data was used to calculate the heat transfer coefficient. For the mass transfer coefficients, a trial and error procedure was used by running simulations with the model and correcting the value of the coefficient according to the obtained

results when compared with experimental results of the total porous fraction.

In the modified Flory−Huggins equation, α, β, and γ were fitted from PEG-35 KDa-water composition experimental data from Wohlfarth.[37,38]

PEG−water solution parameters such as ΔH_m, Cp_m, T_m were calculated as concentration weighted averages.

Table 1. Estimated Parameters

parameter	value
κ, λ	21.35, 0.256
α, β, γ	−378.5, 5.235, 3.8943 × 10^{-3}
k_m	0.0498 m/s^2
h_{wall}	500 W/m K
D_p	1.15 × 10^{-10} m^2/s

PEG with an average molecular weight of 35 kDa has a melting temperature of ca. 331 K according to the manufacturer (Sigma-Aldrich poly(ethylene glycol) 35 000, PN 81310), while water solidifies at 273.15 K. Also, experimental equilibrium measurements of liquid−liquid equilibrium data of PEG (33500)−water solutions at 12.5% w/w PEG/water have been reported at 382 K.[38]

4. RESULTS AND DISCUSSION

The unidirectional freezing process is very complex and has been studied from the experimental viewpoint. From those studies, one can conclude that several parameters such as dissolution concentration, solute molecular weight, freezing front rate, and immersion rate affect the morphology of the final material. The most important effect on pore size is due to freezing front rate, which is the reason to study this parameter in detail through three different freezing methods. Morphology was studied in at least six different zones, and temperature was measured in six zones with thermocouples.

4.1. Freezing Front Rate Effect on the Pore Size. The effect of the freezing conditions on the pore size was studied through scanning electron microscopy (SEM). The freezing conditions were chosen from previous experiments where the initial length of the sample immersed in the LN was varied to fix the natural freezing profiles. The techniques used to study the effect that freezing front rate has on the morphology were LCI 10−30, LCI, and CI-vapors.

LCI 10−30. Figure 2 shows the morphology evolution in the freezing direction for the LCI 10−30 technique; one can observe that the morphology is highly homogeneous except in zone A. Zone A is the first one to be exposed to liquid nitrogen, and a lamellar structure was formed promoted by the quickly movement of the freezing front rate; extremely low temperature leads to rapid formation of ice nuclei and growth of small crystals. The solute promotes heterogeneous nucleation accelerating the nucleation process leading the formation of sites where ice crystals will grow. In zone B, where the immersion started at constant rate, the pore morphology changed from lamellar to honeycomb structures with an average pore size of approximately 8 μm. In general, the immersion rate and the freezing front rate show different time scales, and the idea behind immersing-stopping-immersing is to match both rates to promote homogeneity of the material.

LCI. The freezing front rate decreases as the solution moves away from the LN (Figure 3). Zone A is the closest to LN in which the freezing front is the fastest, and it presents a lamellar-

709

dx.doi.org/10.1021/ie301441j | *Ind. Eng. Chem. Res.* 2013, 52, 706−715
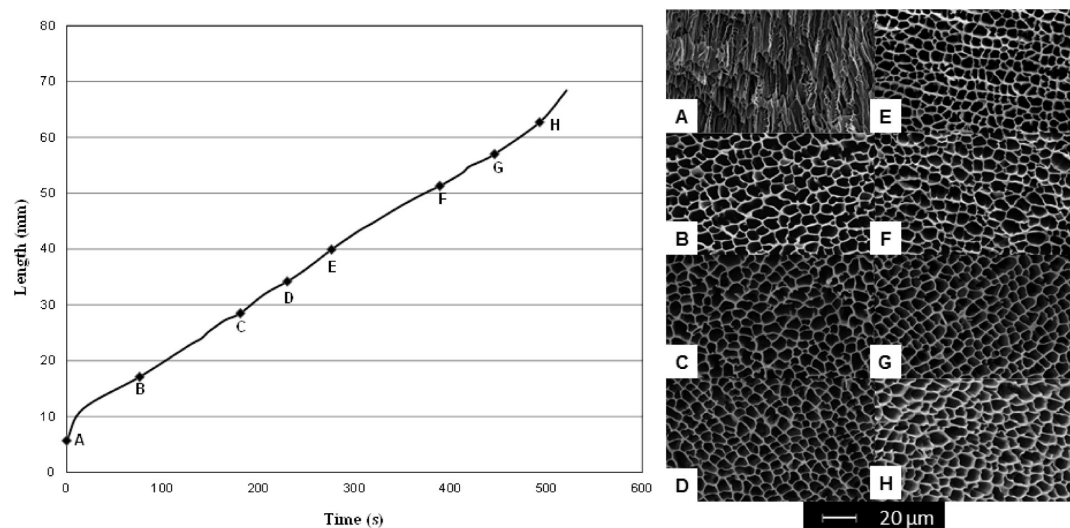
Figure 2. Freezing front rate profile and microstructure LCI 10−30 (A = 5.7 mm, B = 17.1 mm, C = 28.5 mm, D = 34.2 mm, E = 39.9 mm, F = 51.3 mm, G = 57.0 mm, H = 62.7 mm). Scale bar on SEM micrographs is 20 μm.
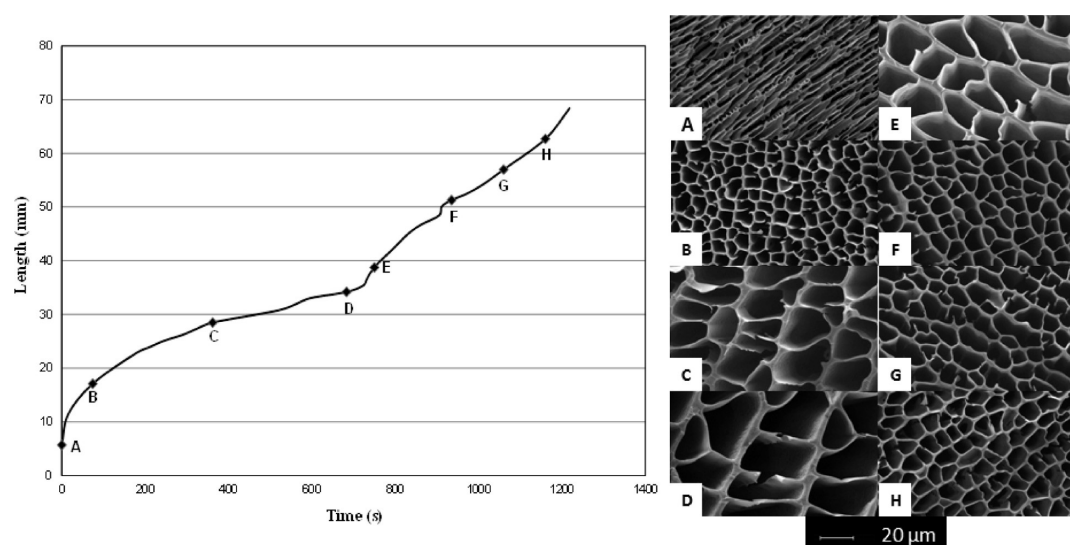

Figure 3. Freezing front rate profile and microstructure for technique LCI (A = 5.7 mm, B = 17.1 mm, C = 28.5 mm, D = 34.2 mm, E = 39.9 mm, F = 51.3 mm, G = 57.0 mm, H = 62.7 mm). Scale bar on SEM micrographs is 20 μm.
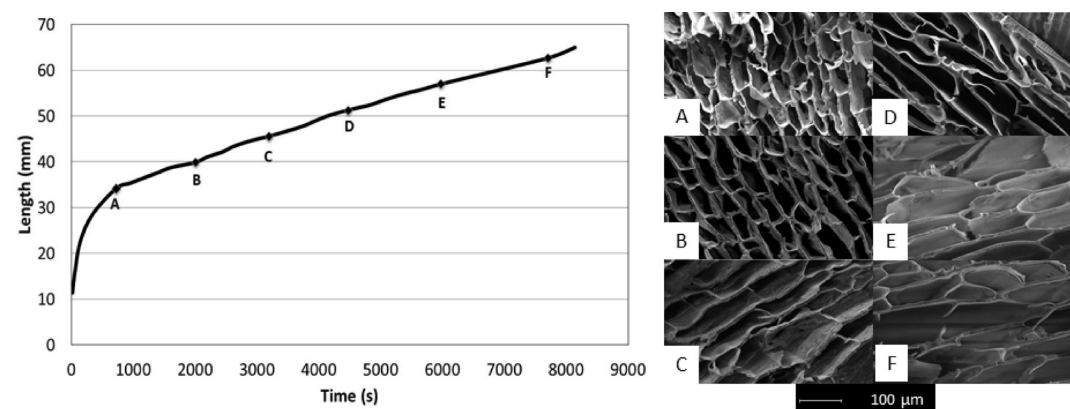
Figure 4. Freezing front rate profile and microstructure CI-vapors (A = 34.2 mm, B = 39.9, C = 45.6, D = 51.3 mm, E = 57.0 mm, F = 62.7 mm). Scale bar on SEM micrographs is 20 μm.

like morphology similarly to the LCI 10−30 technique. The nucleation process is also fast, thus creating more nucleation sites and ice crystal size will be smaller. The freezing front rate diminishes and the size of crystals increases, giving materials
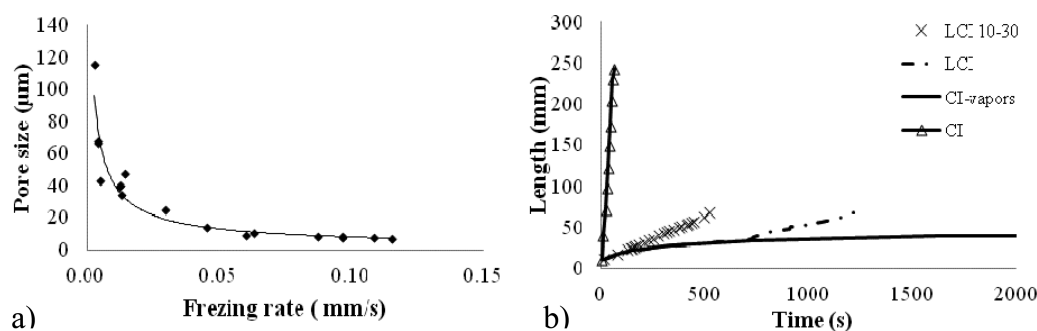
Figure 5. (a) Experimental pore size vs freezing front rate, (b) comparison of the freezing front rate using different techniques (LCI 10−30, LCI, CI-vapors, and constant immersion at 0.24 mm/s.
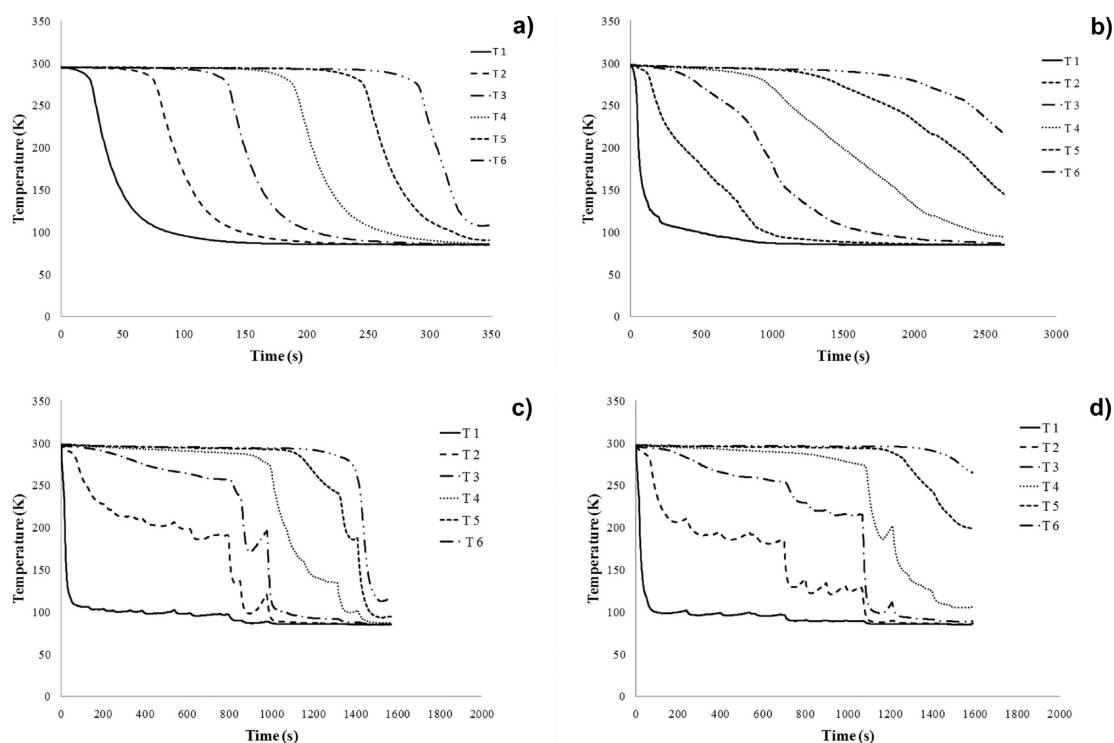
Figure 6. Temperature versus time profile for different freezing techniques: (a) constant immersion at 0.24 mm/s; (b) constant immersion at 0.015 mm/s; (c) LCI 10−30; and (d) CI-vapors.

with bigger pore size. This can be noticed in the zones B to D where pore size increased from 8 to 34 μm. From this point, the sample was immersed in the LN at a constant rate increasing, which effectively increases the freezing front rate. This will produce smaller crystals that in the previous zones. This fact is reflected in zones E to H in which pore size decreases from 34 to 10 μm.

From Figures 2 and 3, one can notice that pore size is inversely proportional to freezing front rate. Varying the immersion rate to promote different freezing front rate is critical to promote different morphologies and pore sizes. For instance, it is very important to produce pores up to 50 μm because many biomedical applications require pores of at least this size (human fibroblasts, keratinocytes, chondrocites are typically ca. 10−50 μm).

CI-vapors. This technique promoted the slowest freezing front rate; the results are shown in Figure 4. Pore size started at 40 μm in zone A and grows to 115 μm in zone E and F. Slow freezing front rate will produce bigger pores.

The "constant immersion" CI technique (as described above) is not shown. However, a general comparison of the effect of freezing front rate on morphology was performed. To obtain this comparison the mean pore size was calculated for each zone and for the four different techniques. Results are shown in Figure 5.

From Figure 5, one can observe, as previously explained, that pore size inversely varies with the freezing front rate. Because the formation of ice crystals starts with a nucleation process, a certain amount of ice nuclei is formed, which can then expand. Ice crystal size is related to freezing front rate: the faster the rate the more nucleation is promoted and greater number of crystals of smaller size will be formed.

At 77 K and ca. 1 atm, amorphous ice is not produced from pure water.[39] Nevertheless, ice crystallization depends on the presence of impurities; in this case, the polymer induced the formation of amorphous ice. When ice is formed, the polymer is expelled from the ice matrix formed; this is another parameter that affects the morphology of ice crystals.
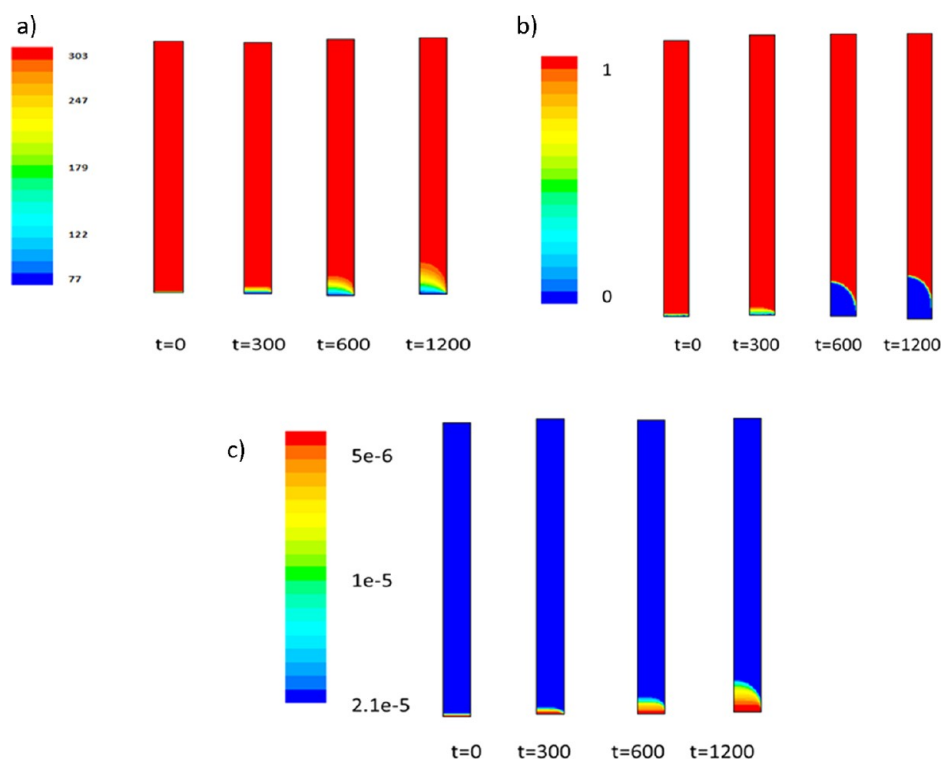
Figure 7. Simulation of the ISISA Process. (a) Temperature profiles (K) at $t = 0$, 300, 600, and 1200 s; (b) liquid to solid phase change (0 = liquid phase, 1 = solid phase), $t = 0$, 300, 600, and 1200 s; (c) porous size (m) $t = 0$, 300, 600, and 1200 s.

4.2. Temperature Profiles. To study the effect of freezing technique on temperature profile three freezing techniques were compared: immersion at a constant rate (0.24 and 0.015 mm/s), LCI 10−30, and CI-vapors. The experimental results are shown in Figure 6.

Temperature profiles were compared by freezing technique and then by zone. From a general perspective, we can observe that the freezing techniques with constant immersion (Figure 6a and b) show homogeneous temperature profiles, faster the process a more homogeneous profile is presented. When aqueous solution is frozen, a large amount of heat (latent heat) is released; if this is not removed from the system as fast as it is released, an elevation in temperature takes place. The sample was continuously immersed in LN, and a bigger area was exposed to this temperature (77 K) removing heat from the system and a temperature increase was not observed. Although the temperature profile for the constant immersion process (0.24 and 0.015 mm/s) was constant, every region reached the lowest temperature at the same rate; the formed material did not have a homogeneous morphology. Qualitatively, crystal size can be predicted from freezing curves (temperature versus time), as it only depends on freezing front rate, which would be affected by immersion rate.

In the LCI 10−30 and CI-vapors techniques (Figure 6c and d), it was allowed that freezing front advances in a natural way. In this case, a small increase in temperature was observed, showing that latent heat was released in the system, and this was not removed fast enough. Compared with the previous cases, this was a slow process. When the sample was immersed into the LN, a marked drop in temperature was observed in the bottom of the sample because medium was cold enough (77 K) to promote advancement of the freezing front; the freezing front rate decreased as the freezing front moved away from the LN because of heat transfer by the surroundings. The slower

freezing front rate and solute added promotes a longer crystal growth stage, with less number of nuclei and crystal of bigger size.

In the CI-vapors (Figure 6d), the first part of the sample was immersed in LN as in the previous case, the characteristic increase in temperature were shown in three thermocouples, and the other half of the sample was frozen by the LN vapors. In this case, the vapors surrounding the sample have a colder temperature than the room where the experiment takes place; this helps develop linear profiles. The freezing front rate in this technique was the slowest studied giving the bigger pores. Not only does the freezing front rate affect crystal size but also the presence of impurities (polymer in this case). When water freezes, the polymer is expelled from the ice matrix that is formed promoting a faster nucleation stage (small crystals).

4.3. Simulations. Numerical solution of the Population balance−Stefan problem is excessive time-consuming compared with the Eulerian−Stefan problem. Therefore, the Eulerian−Stefan problem is preferred if computational facilities are scarce.

The process chosen as reference for modeling purposes is the freezing without immersion, only the bottom of the sample is in contact with liquid nitrogen. Three aspects were simulated along the sample: temperature profile, phase change from liquid to solid, and porous size or ice crystal size.

As stated before, experimental data and properties of polymer and polymer−water solution are scarce. Simulations were made in an axis-symmetrical domain; in the left side of each incise of Figure 7, there is a representation of the sample. In the case of temperature, the top and bottom are fixed to a known temperature, 77 K for the bottom, and the top is set at room temperature. The simulation for the temperature profile is show in (Figure 7a). Nakagawa et al.[33] placed three thermocouples in the sample (surroundings, center, and wall) to study the difference in temperature in the x-region founding

that the front is parabolic. Even when the quantitative behavior is fairly predicted by the model because of the simplifications and the lack of parameters in literature, the qualitative behavior is well predicted. In Figure 7a and b, it can be noticed that a parabolic front is predicted with a maximum in the center of the domain. As expected, because the sides of the representation, the walls of the syringe are set to room temperature. The model successfully predicts the moving of the frozen zone in the up direction.

The Eulerian model predicts the average porosity of the formed void space when PEG–water liquid separates. Size and number are not predicted, diminishing its applicability for a more exact modeling of the process.

Some of the parameters for the population balance simulations were estimated from experimental data. Figure 7c show the pore size predicted by the population balance; even when the parameters used for the model need to be improved with more experimental data, it was predicted with a good accuracy. The predicted mean pore size is overestimated by the PB model in about 35%. This is a good agreement considering the lack of parameters in literature.

Despite the fact that is not possible predict the quantitative behavior of the system, the model successfully predicts the qualitative behavior for the process parameters (temperature profile and change of phase) using the Eulerian model and the pore size through the Population balance model. The case simulated corresponds to the limit case when freezing front rate is close to zero.

Even when the physical system is very complicated and the results obtained by the model only predict the qualitative behavior, the model implemented in this paper can be used as a start point in the modeling of the ISISA process.

4.4. Characterization. *4.4.1. FTIR Analysis.* FTIR characterization of the pristine (PEG bulk) and processed material (PEG scaffold) was performed in a Perkin-Elmer Spectrum One FTIR (Fourier transform infrared) instrument, under transmission mode. These spectra are shown in the bottom of Figure 8, in which it is possible to observe that there is no a significant difference between both spectra in PEG characteristic bands. Both materials exhibits absorptions associated to
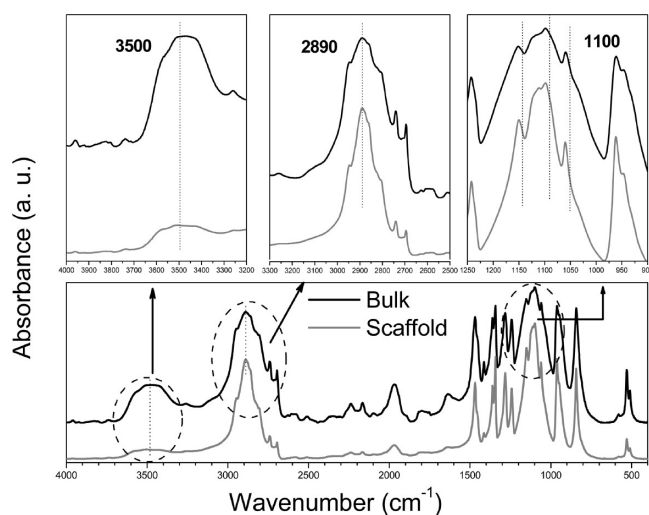
stretching and bending vibrations of C−C, C−O, C−H, and O−H, from methylene and hydroxyl groups. Thus, the broad band around 3500 cm^{-1} is associated to OH stretching vibration; bands around 2880 and 1470 cm^{-1} are assigned to stretch and bending vibrations for methylene group (−CH$_2$−), respectively. PEG presents the typical bands of a primary alcohol in 1340 cm^{-1} due to OH in-plane bending vibration, around 1280 cm^{-1} associated to C−H (from CH−OH) deformation vibration, and close to 1050 cm^{-1} assigned to C−O stretching vibration.[40−42]

There is no evident displacement in the wavenumber comparing both spectra, which indicates that the process to obtain the scaffold had no effects on the PEG structure; however, it is evident that the scaffold spectrum has a lower intensity compared with bulk. This slight, but important, change can be observed specially in the three regions, around 3500, 2890, and 1100 cm^{-1} (vibrations associated to O−H, −CH$_2$−, and C−O, respectively) indicated in dash circles (bottom of Figure 8); each zone is enlarged and magnified in the upper of Figure 8. It is possible to observe that the more significant differences come from the OH region (around 3500 cm^{-1}) where the intensity of this band in the scaffold is less than in bulk, revealing modifications of hydrogen bond in the PEG packing network after the processing.[43,44] This effect can be further corroborated by XRD, where the crystallinity pattern is essentially the same for both materials.

4.4.2. XRD Analysis. XRD patterns are shown in Figure 9. There are two main diffraction peaks around 22° and 27°; this
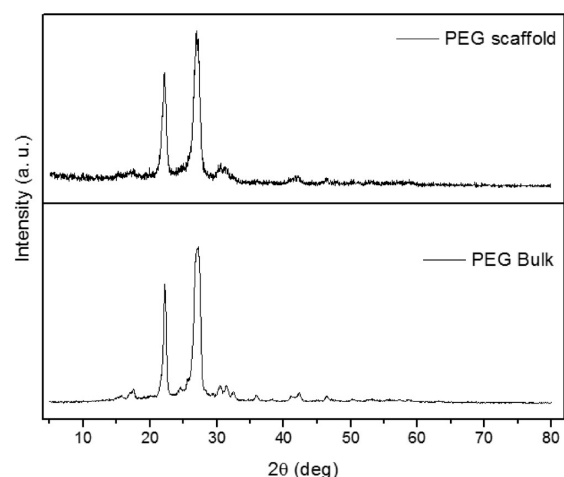
Figure 9. XRD spectra for PEG and PEG scaffold.

behavior indicates that crystalline structure of both materials has not been modified by the ISISA process. The degree of crystallinity was obtained as the ratio of the integrals of the intensities of the crystalline phase and amorphous phase using WinJADE MDI version-6.5 software. For PEG bulk, the volume fraction is 78% while for PEG scaffold is 77%. Because of the very slow rate of immersion in the ISISA process, both nuclei and growth mechanisms in PEG scaffold do not interfere significantly in its crystalline structure compared with PEG bulk.

4. CONCLUSIONS

The elaboration of PEG scaffolds with pore sizes bigger than 50 μm by a unidirectional freezing technique was achieved. The experimental study of this technique provided enough

Figure 8. FTIR spectra showing characteristic bands for the PEG and PEG scaffold. Upper: amplified regions around 3500, 2890, and 1100 cm^{-1}, showing differences in shape and intensity.

information for its optimization. The most influential variable on the pore size of the final material is the freezing front rate. This rate must be controlled during all the process to obtain homogeneous materials. As the freezing front rate increases, smaller pores are obtained.

FTIR characterization of the material unprocessed (PEG bulk) and processed (PEG scaffold) shows that there is no change in the molecular arrangement of the material but in the hydrogen bond formation. This is in agreement with the XRD, where the crystallinity pattern is basically the same for both materials.

The process was modeled using the Eulerian model for the temperature profile and change in phase from liquid to solid. The pore size was modeled using a Population balance model. The qualitative behavior was successfully modeled using this combination. The model presented here can be consider a preliminary model of the process because it only take into account the limit case when the freezing front advance rate is close to zero; however, it can be used as start point for a more complete model that include the immersion of the sample. Because of the lack of parameters in literature more experimental studies are necessary to improve the results of the model.

■ AUTHOR INFORMATION

Corresponding Author
*E-mail: gluna@qro.cinvestav.mx.

Notes
The authors declare no competing financial interest.

■ ACKNOWLEDGMENTS

■ NOMENCLATURE

a_{wall}	heat transfer area
Cp_L	heat capacity at constant pressure of the liquid phase
Cp_M	heat capacity at constant pressure of the mix
C_{PEG}	concentration of PEG
Cp_s	heat capacity at constant pressure of the solid phase
C_{sol}	heat capacity at constant pressure of the concentrated phase
C_W	concentration of water
D_{WP}	water−polymer diffusion coefficient
h_M	latent heat of freezing
h_{wall}	heat transfer coefficient
$J_0(T_c)$	nucleation term
K	Boltzmann constant
k_m	mass transfer coefficient
k'_{ea}	effective conductivity of PEG-water mixture
k'_{el}	effective conductivity of liquid phase
k'_{es}	effective conductivity of solid phase
M	total amount of water dispersed
$m(t)$	mass of crystallized water at time t
N_{PEG}	number of PEG molecules
N_w	number of water molecules
r_{PEG}	number of lattice sites occupied by PEG
r_W	number of lattice sites occupied by water
t	time
T	temperature, Kelvin
T_c	crystallization temperature
T_L	liquid phase temperature
T_m	melting temperature
T_M	mixture temperature
T_S	solid phase temperature
T_{wall}	temperature at the wall, Kelvin
V	volume
$x(t)$	crystallized water at time t

Greek Letters

α	Flory−Huggins constant
β	Flory−Huggins constant
γ	Flory−Huggins constant
ΔG_{mix}	free Gibbs energy
δN_v	number of uncrystallized droplets at $t = 0$
$\delta \acute{N}_v$	number of uncrystallized droplets at time t
ε_{sol}	volume fraction of concentrated phase
ε_w	volume fraction of diluted phase
ρ	density
ρ_L	density of the liquid phase
ρ_M	density of the mixture
ρ_S	density of the solid phase
ρ_{Sol}	density of concentrated phase
ρ_w	density of water
ϕ_{PEG}	volume Fraction of PEG
ϕ_{Sol}	volume fraction of water in concentrated phase
ϕ_w	volume fraction of water in diluted phase
$\xi(x)$	location of liquid solid boundary
$\partial \xi / \partial t$	velocity of advancement of the interphase
χ	Flory−Huggins Parameter

■ REFERENCES

(1) Zhang, H.; Hussain, I.; Brust, M.; Butler, M. F.; Rannard, S. P.; Cooper, A. I. Aligned two- and three-dimensional structures by directional freezing of polymers and nanoparticles. *Nat. Mat.* **2005**, *4*, 787.

(2) Darder, M.; Aranda, P.; Gutierrez, M. C.; Ferrer, M. L.; del Monte, F.; Ruiz-Hitzky, E. Progress in bionanocomposite and bioinspired foams. *Adv. Mater.* **2011**, *23*, 5262.

(3) Ratner, B. D.; Hoffman, A. S.; Schoen, F. J.; Lemons, J. E. *Biomaterials Science, An Introduction to materials in Medicine*, 2nd ed.; Elsevier: San Diego, CA, 1996.

(4) Lin-Gibson, S.; Cooper, J. A.; Landis, F. A.; Cicerone, M. T. Systematic investigation of porogen size and content on scaffold morphometric parameters. *Biomacromolecules* **2007**, *8*, 1511.

(5) Zmora, S.; Glicklis, R.; Cohen, S. Tailoring the pore architecture in 3-D alginate scaffolds by controlling the freezing regime during fabrication. *Biomaterials* **2002**, *23*, 4087.

(6) Deville, S.; Saiz, E.; Nalla, R. K.; Tomsia, A. P. Freezing as a path to build complex composites. *Science* **2006**, *311*, 515.

(7) Nishihara, H.; Mukai, S. R.; Yamashita, D.; Tamon, H. Ordered macroporous silica by ice templating. *Chem. Mater.* **2005**, *17*, 683−689.

(8) Deville, S.; Saiz, E.; Tomsia, A. P. Freeze casting of hydroxyapatite scaffolds for bone tissue engineering. *Biomaterials* **2006**, *27*, 5480.

(9) Ferrer, M. L.; Esquembre, R.; Ortega, I.; Reyes Mateo, C.; del Monte, F. Freezing of binary colloidal systems for the formation of hierarchy assemblies. *Chem. Mater.* **2006**, *18*, 554.

(10) Hortigüela, M. J.; Aranaz, I.; Gutierrez, M. C.; Ferrer, M. L.; del Monte, F. Chitosan gelation induced by the in situ formation of gold nanoparticles and its processing into macroporous scaffolds. *Biomacromolecules* **2011**, *12*, 179.

(11) Romeo, H. E.; Hoppe, C. E.; López-Quintela, M. A.; Williams, R. J. J.; Minaberry, M.; Jobbágy, M. Directional freezing of liquid crystalline systems: From silver nanowire/PVA aqueous dispersions to highly ordered and electrically conductive macroporous scaffolds. *J. Mater. Chem.* **2012**, *22*, 9195.

(12) Mi, X.; Wang, W.; Gao, J.; Long, Y.; Xing, F.; Wang, F.; Xu, F.; You, X.; Li, S.; Liu, Y. Fabrication of highly porous starch monoliths and their application as green desiccants. *Polym. Adv. Technol.* **2012**, *23*, 38.

(13) Wang, X.; Kong, W.; Xie, W.; Li, L.; Liu, Y.; Wu, X.; Gao, J. Bi-porous bioinspired chitosan foams with layered structure and their adsorption for xylenol orange. *Chem. Eng. J.* **2012**, *197*, 509.

(14) Zhang, Y.; Choi, S.-W.; Xia, Y. Modifying the pores of an inverse opal scaffold with chitosan microstructures for truly three-dimensional cell culture. *Macromol. Rapid Commun.* **2012**, *33*, 296.

(15) Ferrer, M. L.; Garcia, Z. Y.; Yuste, L.; Rojo, F.; del Monte, F. Bacteria viability in sol-gel materials revisited: Cryo-SEM as a suitable tool to study the structural integrity of encapsulated bacteria. *Chem. Mater.* **2006**, *18*, 1458.

(16) Gutierrez, M. C.; Jobbágy, M; Rapún, N.; Ferrer, M. L.; del Monte, F. A biocompatible bottom-up route for the preparation of hierarchical biohybrid materials. *Adv. Mater.* **2006**, *18*, 1137.

(17) Gutierrez, M. C.; García, Z. Y.; Jobbágy, M.; Yuste, L.; Rojo, F.; Abrusci, C.; Catalina, F.; del Monte, F.; Ferrer, M. L. Hydrogel scaffolds with immobilized bacteria for 3D cultures. *Chem. Mater.* **2007**, *19*, 1968.

(18) Gutierrez, M. C.; García, Z. Y.; Hortigüela, M. J.; Yuste, L.; Rojo, F.; Ferrer, M. L.; del Monte, F. Biocompatible MWCNT scaffolds for immobilization and proliferation of E. coli. *J. Mater. Chem.* **2007**, *17*, 2992.

(19) Nardecchia, S.; Serrano, M. C.; Portolés, M. T; Gutierrez, M. C.; Ferrer, M. L.; del Monte, F. Osteoconductive performance of carbon nanotube scaffolds homogeneously mineralized by flow-through electrodeposition. *Adv. Funct. Mater.* **2012**, DOI: 10.1002/adfm.201200684.

(20) Abarrategi, A.; Gutierrez, M. C.; Moreno-Vicente, C.; Hortigüela, M. J.; Ramos, V.; López-Lacomba, J. L.; Ferrer, M. L.; del Monte, F. Multiwall carbon nanotube scaffolds for tissue engineering purposes. *Biomaterials* **2008**, *29*, 94.

(21) He, Z.; Liu, J.; Qiao, Y.; Li, C. M.; Tan, T. T. Y. Architecture engineering of hierarchically porous chitosan/vacuum-stripped graphene scaffold as bioanode for high performance microbial fuel cell. *Nano Lett.* **2012**, DOI: 10.1021/nl302175j.

(22) Mi, X.; Huang, G.; Xie, W.; Wang, W.; Liu, Y.; Gao, J. Preparation of graphene oxide aerogel and its adsorption for Cu^{2+} ions. *Carbon* **2012**, *50*, 4856.

(23) Zhang, N.; Qiu, H.; Si, Y.; Wang, W.; Gao, J. Fabrication of highly porous biodegradable monoliths strengthened by graphene oxide and their adsorption of metal ions. *Carbon* **2011**, *49*, 827.

(24) Spender, J.; Demers, A. L.; Xie, X.; Cline, A. E.; Earle, M. A; Ellis, L. D.; Neivandt, D. J. Method for production of polymer and carbon nanofibers from water-soluble polymers. *Nano Lett.* **2012**, *12*, 3857.

(25) Gutierrez, M. C.; Jobbágy, M.; Ferrer, M. L.; del Monte, F. Enzymatic synthesis of amorphous calcium phosphate chitosan nanocomposites and their processing into hierarchical structures. *Chem. Mater.* **2008**, *20*, 11.

(26) Vickery, J. L.; Patil, A. J.; Mann, S. Fabrication of graphene-polymer nanocomposites with higher-order three-dimensional architectures. *Adv. Mater.* **2009**, *21*, 2180.

(27) DeVille, S.; Saiz, E.; Tomisa, A. P. Ice-templated porous alumina structures. *Acta Mater.* **2007**, *55*, 1965.

(28) Gutierrez, M. C.; García, Z. Y.; Jobbágy, M; Rubio, F.; Yuste, L.; Rojo, F.; Ferrer, M. L.; del Monte, F. Poly(vinyl alcohol) scaffolds with tailored morphologies for drug delivery and controlled release. *Adv. Funct. Mater.* **2007**, *17*, 3505.

(29) Yao, X.; Yao, H.; Li, Y. Hierarchically aligned porous scaffold by ice-segregation-induced self-assembly and thermally triggered electro-static self-assembly of oppositely charged thermosensitive microgels. *J. Mater. Chem.* **2009**, *19*, 6516.

(30) Kim, J.; Taki, K.; Nagamine, S.; Ohshima, M. Preparation of porous poly(L-lactic acid) honeycomb monolith structure by phase separation and unidirectional freezing. *Langmuir* **2009**, *25*, 5304.

(31) Worster, M. G.; Wettlaufer, J. S. Natural convection, solute trapping, and channel formation during solidification of saltwater. *J. Phys. Chem. B* **1997**, *101*, 6132.

(32) Gutiérrez, M. C.; Ferrer, M. L.; del Monte, F. Ice-templated materials: Sophisticated structures exhibiting enhanced functionalities obtained after unidirectional freezing and ice-segregation-induced self-assembly. *Chem. Mater.* **2008**, *20*, 634.

(33) Nakagawa, K; Hottot, A.; Vessot, S; Andrieu, J. Modeling of freezing step during dreeze-drying of drugs in vials. *AIChE J.* **2007**, *53*, 1362.

(34) Nakagawa, K.; Thongprachan, N.; Charinpanitkuli, T.; Tanthapanichakoon, W. Ice crystal formation in the carbon nanotube suspension: A modeling approach. *Chem. Eng. Sci.* **2010**, *65*, 1438.

(35) Nakagawa, K; Surassmo, S; Min, S-G; Choi, M.-J. Dispersibility of freeze-dried poly(epsilon-caprolactone) nanocapsules stabilized by gelatin and the effect of freezing. *J. Food Eng.* **2011**, *102*, 177.

(36) Ramkrishna, D. *Population Balances: Theory and Applications to Particulate Systems in Engineering*; Academic Press: San Diego, CA, 2000.

(37) Wolfhart, C. *Handbook of Thermodynamic Data of Aqueous Polymer Solutions*; CRC Press: Boca Raton, FL, 2004.

(38) Wolfhart, C. *Handbook of Liquid-Liquid Equilibrium Data of Polymer Solutions*; CRC Press; Boca Raton, FL, 2008.

(39) Debenedetti, P. G.; Stanley, H. E. Supercooled and glassy water. *Phys. Today* **2003**, *56*, 40.

(40) Reddy, P. A.; Kuman, R. Impedance spectroscopy and FTIR studies of PEG-based polymer electrolytes. *J. Chem.* **2011**, *8*, 347.

(41) Lin-vien, D.; Colthup, B. N.; Ateley, G. W.; Graseelli, G. J. *The Handbook of Infrared and Raman Characteristics Frequencies of Organic Molecules*; Academic Press: San Diego, CA, 1991.

(42) Pretsch, E.; Simon, W.; Seibl, J.; Clerc, T. *Tables of Spectral Data for Structure of Organic Compounds*; Springer-Verlag: Weinheim, Germany, 1989.

(43) Turhan, K. N.; Sahbaz, F.; Güner, A. A spectrophotometric study of hydrogen bonding in methylcellulose-based edible films plasticized by polyethylene glycol. *J. Food Sci.* **2001**, *66*, 59.

(44) Zhang, J.; Han, F.; Wei, X.; Shui, L.; Gong, H.; Zhang, P. Spectral studies of hydrogen bonding and interaction in the absorption processes of sulfur dioxide in poly(ethylene glycol) 400 + water binary system. *Ind. Eng. Chem. Res.* **2010**, *49*, 2025.